Paint With the Sun: A Thermal-Vision Guided Robot to Harness Solar Energy for Heliography

Luyin Hu, Anqing Duan, Mengying Li, Andrea Cherubini, Lu Li, and David Navarro-Alarcon, *Senior Member, IEEE*

Abstract—In this article, we present a novel robotic system for heliography, which literally refers to painting with the Sun. In the context of artistic creation, heliography involves the precise manipulation of a magnifying glass to burn artwork on wooden panels by concentrating solar energy. Since this painting procedure exposes the human operator to prolonged periods of intensive sunlight, it can potentially cause sunburns to the skin or damage the eyes. To avoid these issues, in this article, we propose to automate the heliography process with a robot in lieu of a human operator. The proposed thermal servoing capabilities have the potential to robotize various solar power generation technologies such as concentrated solar power (CSP) and concentrated photovoltaics (CPVs). To perform this task, our robotic system is equipped with a magnifying glass attached to the end-effector and is instrumented with vision and thermal sensors. The proposed sensor-based controls enable to automatically: 1) track the orientation of the Sun in real time to maximize the concentrated solar energy; 2) direct the solar rays toward the point of interest; and 3) control the heat power intensity at the target point to achieve the required steady-state temperature. The performance of our system is evaluated by conducting autonomous heliography experiments with various patterns.

Developed System — System Schematics — Geometric Optics — Heliography Experiments

Index Terms—Robotic manipulation, sensor-based control, solar energy, thermoception, visual servoing.
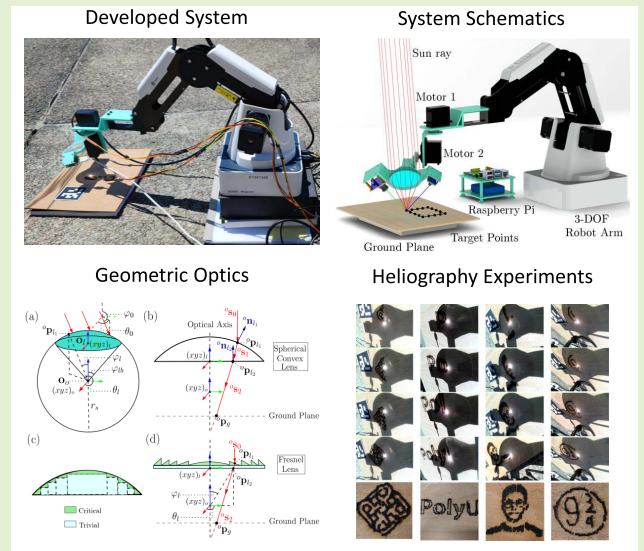
NOMENCLATURE

$\mathbf{p}^*_{i=1,\dots,k}$	ith target point for solar concentration.
$\mathbf{p}_{l_1}$, $\mathbf{p}_{l_2}$	Point on the lens' convex and flat boundary.
$\mathbf{p}_g$	Intersection point between $\mathbf{s}_2$ and the ground plane.
$\mathbf{p}^*_g$	Corresponding point of a pixel through homography.
$\mathbf{s}_0, \mathbf{s}_1, \mathbf{s}_2$	Incident Sun ray and the refracted Sun rays.
φ_l, θ_l	Lens polar angle and lens azimuthal angle.
φ_0, θ_0	Solar polar angle and solar azimuthal angle.
$\mathbf{n}_{l_1}, \mathbf{n}_{l_2}$	Normal of the lens' convex and flat boundary.
$\mathbf{n}_g$	Normal vector to the ground plane.
Π, Θ	Geometric features of the concentrated light spot.
$\mathbf{y}$	Feature vector $\mathbf{y} = [\Pi, \Theta]^\mathsf{T}$.
$\mathbf{y}_{\text{img}}$	Feature $\mathbf{y}$ computed from the image feedback.
$\mathbf{y}^t$	Feature $\mathbf{y}$ computed at step t of the simulation.
φ_0^t, θ_0^t	φ_0 and θ_0 updated at step t of the simulation.
$\boldsymbol{\vartheta}^t$	$\vartheta^t = [\varphi_0^t, \theta_0^t]^\mathsf{T}$: solar angles updated at step t.
$\widehat{\boldsymbol{\vartheta}}$	Final estimation of $\boldsymbol{\vartheta}$ when the simulation terminates.
T_p	Wood pyrolysis temperature.
$T_c^{\max}$	Maximum temperature from a thermal image feedback.
d_{lp}	Distance between a target point and the lens center.
N_p	Number of thermal image pixels that indicate pyrolysis.

I. INTRODUCTION

IN THE context of art production, heliography is a technique that consists in concentrating—with the aid of mirrors and lenses—solar rays on wooden surfaces to create artworks [1]. Unlike painters, who draw on a canvas using a paintbrush, heliographic artists rely on the focal point that results from the refraction of sunlight passing through a magnifying glass. This focal point possesses a high energy flux that enables the artist to carbonize the wood and leave patterns, similar to a paintbrush. Fig. 1(a) shows an example of a traditional heliographic artwork produced by manipulating the focal point on a wood canvas. Such a procedure requires precise manipulation skills since both the focus duration and the projection distance affect the quality of the artwork; a long focus duration will burn through the wood, while a deviated projection distance will not produce the desired width of the burning trace.

To produce a complete art piece may take an artist anything between a couple of hours to several weeks, depending on the size, level of detail, and employed materials. While creating the desired pattern, the artist may undergo prolonged periods of direct exposure to sunlight and its ultraviolet radiation, which can cause various skin and eye problems, e.g., sunburns, melanoma, or even cataracts. As a feasible solution to these issues, we propose to automate heliography with a robotic system that controls the Sun concentration process, effectively taking over the role of the artist [see Fig. 1(b)]. The sensorimotor controls that are needed to produce this type of artwork are also valuable from a renewable energy perspective (e.g., robotic structures can automate the harnessing of solar energy in a concentrated solar power system). Conceivably, robots with the capability to exploit off-the-peg energy sources from the environment can potentially save a considerable amount of energy. Our aim in this article is precisely to develop the necessary models and methods for robots to achieve this level of thermomotor intelligence.

From an application perspective, there is a large volume of literature dedicated to robotizing tasks such as painting, drawing, and brushing, whose spatial trajectories are similar to those used in heliography. For example, to teach a robot the skill of performing esthetic calligraphy, a controller can reproduce the strokes captured from previous human writing demonstrations [3]. Similarly, artistic portraits can be realized by processing images of human faces and then planning trajectories to be followed by a robot-held drawing device [4]. Different from the aforementioned painting robots [5], our system does not need any ink or pigment to leave traces on a canvas; instead, it relies on the carbonization of a wooden panel. Similar working principles can be found in systems that manipulate lasers [6], which have been used to create various types of artworks [7], [8]. Compared with these laser-based painting systems, our robot does not require any external power supply to carbonize the surface.

We highlight that one salient aspect of our proposed system is exploitation of solar energy, an important topic in various fields due to its sustainable and eco-friendly nature.

Fig. 1. Illustration of heliography performed by (a) artist [2] and (b) robotic arm.

One popular application is the so-called solar cooker that can process food or boil water by converting solar energy into heat [9]. Our system exploits solar energy to carbonize the wooden panel, and unlike the solar cooker, it needs faster and more precise temperature controls to avoid burning through the wood. Many mobile robotic systems power their motion by adjusting the pose of onboard photovoltaic panels so as to maximize the incidence of solar rays over its surface [10], [11], a condition analogous to our rays-lens alignment problem.

The heliography process requires us to maximize the amount of solar rays passing through the magnifying glass, which is achieved by tracking the Sun's direction [12]. To this end, we design an iterative strategy that estimates the Sun's direction by visually measuring the projected shadow feature of the lens; at the core of this approach is the system's interaction matrix that captures the relationship between the Sun direction increments and the feature vector increments. Compared with alternative approaches for Sun direction inference based on specialized sensors (digital compass [13], catadioptric camera [14], and light-dependent resistors [15]) or based on deep neural networks (which require large datasets [16]), our proposed sensor-based solution is simple to implement and data efficient.

For the robot to automate the task, real-time acquisition of the surrounding environment states is essential [17]. In our application, two states are considered to play an important role in the success of the task: 1) location of the solar focal point and 2) temperature of the projected focal point over the surface. The former suggests installation of an RGB camera to visually track the projected 2-D point [18], [19], while the latter suggests installation of a thermal camera to monitor its temperature [20], [21]. The integration of thermal and visual information to augment robot capabilities has been recently studied in many works, e.g., human falling detection [22], thermographic reconstruction [23], and spacecraft operations [24]. In this work, we show how thermal and visual signals can be used to guide the end-effector's motion, thus paving a new path toward the development of multiperception modalities for robotic manipulation [25], [26].

The original contributions of this article are given as follows:

1) a new sensor-based Sun tracking algorithm to collect a maximum amount of solar energy with the lens;
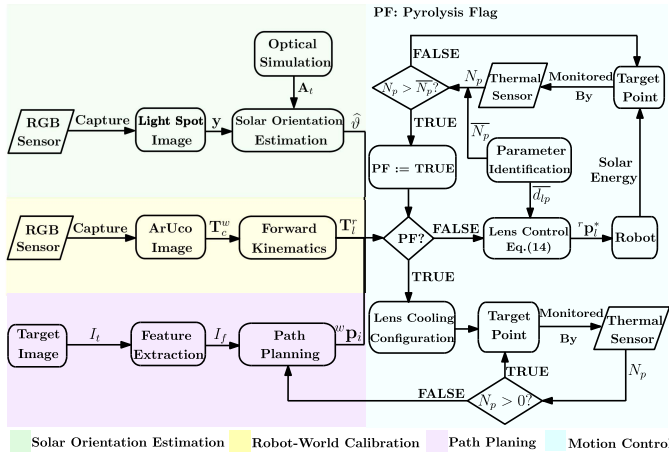2) a new motion planning strategy to direct and concentrate the Sun's rays over a point of interest;

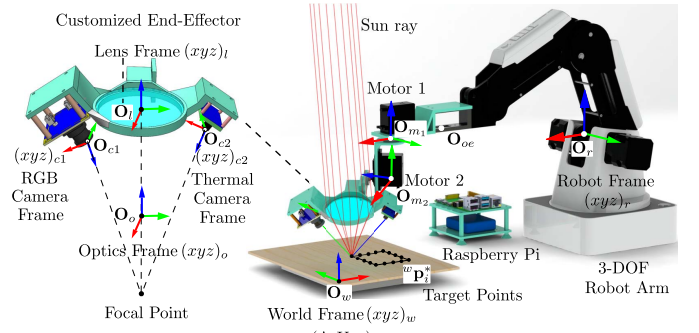Fig. 2. Workflow of the proposed robotic painter.

Fig. 3. Schematic of the system with relevant frames. The system is composed of a 3-DOF robot arm with two additional motors (controlled by a Raspberry Pi), manipulating a customized end-effector. The end-effector carries a spherical Fresnel lens, an RGB camera, and a thermal camera. An ArUco marker defines the world frame.

3) a new sensor-based control law to regulate the temperate at the target point and achieve a desired steady state or an appropriate heating process.

II. PRELIMINARIES

Notation: Throughout this article, we denote all column vectors by lower bold case letters, e.g., $\mathbf{r} \in \mathbb{R}^{n \times 1}$, and matrices by bold capital letters, e.g., $\mathbf{T} \in \mathbb{R}^{m \times n}$. We use a left superscript to indicate the coordinate system of a homogeneous position vector, e.g., $^a\mathbf{r} \in \mathbb{R}^{4 \times 1}$ is expressed in frame $(xyz)_a$. The axes of $(xyz)_a$ are denoted by $\mathbf{x}_a$, $\mathbf{y}_a$, and $\mathbf{z}_a$, respectively. A matrix $\mathbf{T}_b^a \in \mathbb{R}^{4 \times 4}$ describes the homogeneous transformation from frame $(xyz)_a$ to frame $(xyz)_b$. The trigonometric functions $\sin \theta$ and $\cos \theta$ are abbreviated as $S\theta$ and $C\theta$, respectively. The key notation used in this article is summarized in the Nomenclature.

A. Problem Formulation

Fig. 2 shows an overview of the proposed workflow of our method. The names of the blocks are italicized in the rest of this section. The robotic heliography process consists in concentrating solar energy at a group of target positions in the world frame $P_w = \{^w\mathbf{p}_1^*, \dots, {}^w\mathbf{p}_k^*\}$. These positions are obtained by performing feature extraction and automatic scaling on an input image I_t (i.e., the target figure), which generates the corresponding ordered group of points [27]. Humans achieve this task by manipulating the lens' configuration according to past experience and current observations. To reproduce such functionality with a robot, we analyze the lens' optical principle and developed a ray-tracing optical simulation. This simulation sets the ground for an image-based method to estimate the solar orientation and to compute the required lens' configuration that concentrates solar energy at $^w\mathbf{p}_i^*$. To create the desired patterns, we develop a path planning algorithm, which considers the operation time and the overlap between subsequent target positions.

Alongside the coupling between the robot configuration and the position where solar energy is concentrated, another key aspect of our problem is the heat transfer process occurring at $^w\mathbf{p}_i^*$. The charred regions that appear on the wood's surface result from pyrolysis [28], a reaction that is triggered when the temperature exceeds a certain value. In heliography, it is critical to track the pyrolysis process to avoid underheating/overheating the surface; humans detect this by observing the emerging smoke. However, it is complicated for a robot to visually detect smoke due to the intense light arising from the process. Instead, in our proposed method, we equip the robot with a near infrared thermal camera to directly measure the surface's temperature profile. This sensor feedback is processed to search for the maximum temperature value, which is then sent to the robot's motion controller.

B. Proposed Sensor-Based Robotic System

The main components of the proposed system are shown in Fig. 3. Two servo motors are attached to the end-effector of a three-degree-of-freedom (DOF) robot arm Dobot Magician, to enable the control of 5-DOF poses. A spherical Fresnel lens is manipulated by the robot to concentrate on solar energy, with an RGB camera and a thermal camera rigidly attached to it to monitor the process. The mechanical structure of the end-effector is designed so that the optical axis of the Fresnel lens and the optical axes of the two cameras intersect at the theoretical focal point. Such a design makes the target solar concentration point to appear at the center of the images, which improves the accuracy of the feature recovery process. The lens' yaw and pitch angles are independently controlled by motors 1 and 2, while its 3-DOF translation is controlled by the robotic arm. The joint configuration of the system is denoted by $\mathbf{x} \in \mathbb{R}^5$. Based on the robot's kinematics, we can set the distance between the lens' center and a target point over a plane along with the lens' axis.[1]

We denote the static robot base frame by $(xyz)_r$ and the world frame (which is determined by an ArUco marker attached to the ground plane) by $(xyz)_w$. We denote the origin of the lens frame $(xyz)_l$ by $\mathbf{O}_l$ and set it at the center of the

---

[1]Provided that such desired pose is within the robot reachable workspace.
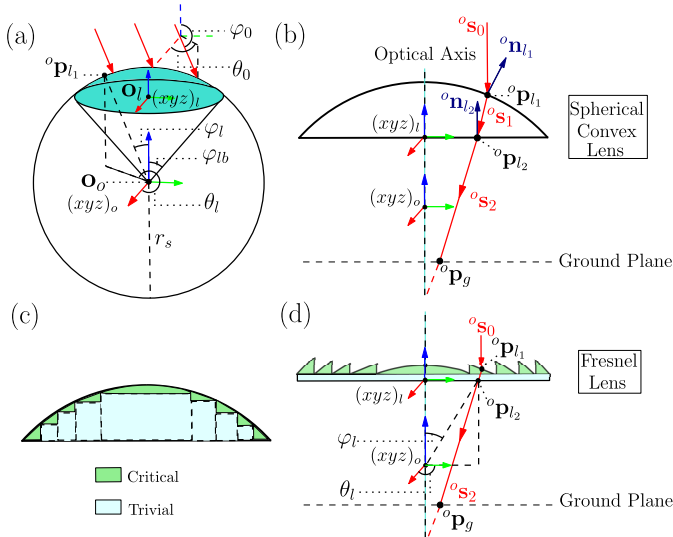
Fig. 4. Ray tracing and structure diagrams of the plano-convex lens and the Fresnel lens. (a) Annotations of the ray refraction in the spherical coordinate. (b) Path of the ray in the convex-plano spherical lens. (c) Illustration of the Fresnel lens design. (d) Path of the ray in the Fresnel lens.

lens upper surface. The axes of $(xyz)_l$ are aligned with the axes of $(xyz)_r$, which defines the origin of the lens yaw angle (the angle between the axis $\mathbf{y}_l$ and the plane $\mathbf{x}_r\mathbf{y}_r$) and the lens pitch angle (rotation around the axis $\mathbf{x}_r$). The RGB camera frame $(xyz)_{c1}$ and the thermal camera frame $(xyz)_{c2}$ are set according to the conventions from [29]. Based on the system's kinematics, the robot-lens transformation matrix $\mathbf{T}_l^r$ can be derived. Since the cameras and the Fresnel lens are rigidly attached to the end-effector, $\mathbf{T}_{c1}^l$, $\mathbf{T}_{c2}^l$, and $\mathbf{T}_{c2}^{c1}$ are known constant matrices. At the beginning of each solar painting task, the world-robot transformation matrix $\mathbf{T}_r^w$ is obtained by observing the ArUco marker attached to the ground plane.

III. SOLAR ORIENTATION ESTIMATION

A. Geometric Optics

In this section, we present the development of our ray-tracing model, which is a critical part of the motion controller. We include the necessary definitions and derivations to simulate ray tracing in solar painting tasks. Interested readers may refer to [30] for more information.

The manipulated Fresnel lens relies on the same working principle as traditional spherical convex lenses. Yet, it is more efficient in terms of cost and energy transmission, ascribed to its specialized design [31]. As shown in Fig. 4(a), the curvature design of a convex lens is based on a sphere with center $\mathbf{O}_o$ and radius r_s as a reference. The region of interest (colored in turquoise) is confined by the lens azimuthal angle $\theta_l \in [0, 2\pi)$ and by the lens polar angle $\varphi_l \in [0, \varphi_{lb}]$, where φ_{lb} is a constant lens bounding polar angle. Fig. 4(b) shows that the incident and refracted rays are denoted by $^o\mathbf{s}_0$, $^o\mathbf{s}_1$, and $^o\mathbf{s}_2$ under the optics frame $(xyz)_o$. The rays only refract at the boundary surface, and hence, the inner part [colored in light blue in Fig. 4(c)] barely contributes to concentration; thus, it can be removed to alleviate energy loss. The final design of the Fresnel lens exploiting this feature is shown in

Fig. 4(d), where the critical curved surface (colored in green) is divided into pieces and placed on the flat boundary surface.

Following the conventions in [30], the origin of the optics frame $(xyz)_o$ is set at the center of the reference sphere. We set the axes of $(xyz)_o$ to be parallel to the axes of $(xyz)_l$. Since the thickness of the Fresnel lens is small (2 mm in this study), to simplify the derivation, we fairly assume that the Sun ray enters and leaves the lens at the same point [see Fig. 4(d)]. Consequently, the position of an incident point $^o\mathbf{p}_{l_1}$ and its corresponding leaving point $^o\mathbf{p}_{l_2}$ are expressed (using homogeneous four vectors [29]) as follows:

$$^o\mathbf{p}_{l_1} = {}^o\mathbf{p}_{l_2} = \begin{bmatrix} p_{l_{1x}} & p_{l_{1y}} & p_{l_{1z}} & 1 \end{bmatrix}^\mathsf{T}$$
$$= \begin{bmatrix} r_s S\varphi_l C\theta_l & r_s S\varphi_l S\theta_l & r_s C\varphi_{lb} & 1 \end{bmatrix}^\mathsf{T}. \quad (1)$$

The directional incident ray is denoted as

$$^o\mathbf{s}_0 = \begin{bmatrix} S\varphi_0 C\theta_0 & S\varphi_0 S\theta_0 & C\varphi_0 & 0 \end{bmatrix}^\mathsf{T} \quad (2)$$

where $\varphi_0 \in [(\pi/2), \pi)$ and $\theta_0 \in [0, 2\pi]$ are the ray polar angle and the ray azimuthal angle [see Fig. 4(a)], respectively. For an incident point $^o\mathbf{p}_{l_1}$ on the convex boundary and an incident point $^o\mathbf{p}_{l_2}$ on the flat boundary, the corresponding active surface normals are [see Fig. 4(b)]

$$^o\mathbf{n}_{l_1} = \begin{bmatrix} S\varphi_l C\theta_l & S\varphi_l S\theta_l & C\varphi_l & 0 \end{bmatrix}^\mathsf{T}$$
$$^o\mathbf{n}_{l_2} = \begin{bmatrix} 0 & 0 & 1 & 0 \end{bmatrix}^\mathsf{T}. \quad (3)$$

The incident angle between $^o\mathbf{s}_0$ and the convex boundary normal $^o\mathbf{n}_1$ is calculated as $\gamma_1 = \arccos(-^o\mathbf{s}_0 \cdot {}^o\mathbf{n}_{l_1})$. To obtain the refracted ray $^o\mathbf{s}_1$, we first define

$$\omega_1 = N_1 C\gamma_1 - \sqrt{1 - N_1^2 + (N_1 C\gamma_1)^2} \quad (4)$$

for $N_1 = \xi_0/\xi_1$ with ξ_0 and ξ_1 as the refractive indices (relative to a specific light wavelength) of the air and the lens material, respectively. Then, $^o\mathbf{s}_1$ can be calculated as [30]

$$^o\mathbf{s}_1 = \begin{bmatrix} s_{1_x} & s_{1_y} & s_{1_z} & 0 \end{bmatrix}^\mathsf{T} = \omega_1 {}^o\mathbf{n}_{l_1} + N_1 {}^o\mathbf{s}_0 \quad (5)$$

while the refracted ray $^o\mathbf{s}_2$ can be similarly calculated as in the procedure above. After the ray leaves the lens's flat boundary, it travels rectilinearly until hitting the ground plane, whose normal direction is denoted by $^o\mathbf{n}_g$. We denote the intersection point of $^o\mathbf{s}_2$ with this plane by

$$^o\mathbf{p}_g = {}^o\mathbf{p}_{l_1} + K {}^o\mathbf{s}_2 \quad (6)$$

where K represents the scaling factor of $^o\mathbf{s}_2$. For a point $^o\mathbf{p}_{go} = [0, 0, d, 1]^\mathsf{T}$ in the ground plane, we can calculate K by solving the equation $(^o\mathbf{p}_g - {}^o\mathbf{p}_{go}) \cdot {}^o\mathbf{n}_g = 0$. This enables to obtain the analytical expression for $^o\mathbf{p}_g$, which is a function of the following variables.

1) The direction of the incident ray $^o\mathbf{s}_0$, which depends on φ_0 and θ_0 according to (2). In this study, φ_0 is related to the Sun elevation angle and θ_0 is related to the Sun azimuthal angle, which varies with time.[2]

[2]The Sun elevation angle is the angular height of the Sun, which is equal to 0 at sunrise. The Sun azimuthal angle is the angle between the projection of the Sun's center onto the horizontal plane and the due north for the northern hemisphere [32]. The solar orientation under this conventional coordinate system can be easily obtained given the longitude, latitude, and time information. However, as the orientation of the robot frame with respect to north is unknown, the solar orientation under the robot frame requires further estimation.
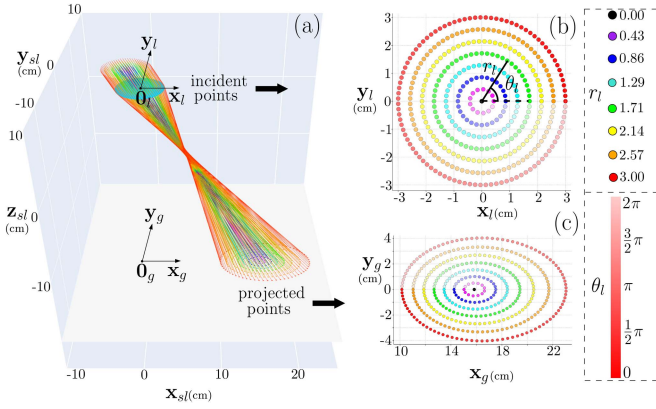
Fig. 5. Illustration of the geometrical characteristics of the projected points. (a) Simulation of the solar concentration with polar angle $\varphi_0 = 5/6\pi$ and azimuthal angle $\theta_0 = 0$. (b) Uniformly sampled incident points on the lens plane. (c) Corresponding projected points on the ground plane.

2) The point where the ray hits the lens, which is parameterized by φ_l and θ_l. In Section III-B, we introduce a group of incident positions that simplify its computation.
3) The relative configuration between the lens plane and the ground plane, which is described by $\mathbf{T}_l^{c1}$ and can be controlled by the robot's motion.

B. Ray-Tracing Simulation Method

To analyze and exploit the coupling between the controllable lens configuration and the solar orientation, we developed a visualization tool based on the aforementioned derivation with the Python Plotly library [33]. An illustration of our ray-tracing method is shown in Fig. 5, where the solar incident angles are set to $\varphi_0 = 5\pi/6$ and $\theta_0 = 0$, the ground plane normal is set to $^o\mathbf{n}_g = [0, 0, 1, 0]^{\mathsf{T}}$, and the lens surface is parallel to the ground plane. To generate a set of uniformly distributed incident points, we pick a series of lengths r_{l_i} that are evenly distributed from 0 to $r_s C\varphi_{lb}$ (the lens radius), where different values of r_{l_i} are represented by different colors. For each circle of radius r_{l_i}, we select sampling points with an equal adjacent θ_l to be visualized. The values of θ_l of the selected points are shown with varying color saturations. As shown in Fig. 5(a), the parallel Sun rays first converge and then diverge after passing through the lens. Fig. 5(b) shows the incident points on the circular lens surface, while Fig. 5(c) shows the projected points over the ground plane.

Our ray-tracing method shows that for a group of incident points $^o\mathbf{p}_{l_1}$ with the same r_{l_i}, their corresponding projected points $^o\mathbf{p}_g$ form a (noncircular) closed contour over the ground plane. Note that for the group of incident points with the largest r_l [shown in red in Fig. 5(b)], the corresponding projected points also form the outermost closed contour in Fig. 5(c). These correspondences allow us to analyze only a representative group of incident points with the same r_{l_i}. The same geometric features can be extracted from the representative as using all the points, while less computing power is required. Based on this observation, we utilize the geometric characteristics (centroid and orientation) of the outermost boundary of the projected light spot for solar

orientation estimation, which can be computed from the visual feedback.

C. Image-Based Solar Orientation Estimation

To automatically align the lens with the Sun ray's direction, we developed an efficient method that estimates the Sun's orientation based on feedback images. To this end, it is important to note that the ground projection point $^o\mathbf{p}_g$ is coupled with the unknown Sun orientation and the known lens-ground relative configuration. Our strategy is to estimate the solar orientation based on images of this point and on the kinematic relationship between $^o\mathbf{p}_g$ and φ_0 and θ_0, which is obtained from the ray-tracing model.

Consider a 2-D image captured by the camera mounted on the end-effector. We segment the image pixels that represent the projected Sun spot by first transforming the image into grayscale and then applying a binary threshold to find the spot's region [34]. To relate the real-world sensor data with the numerical model, we must compute $^o\mathbf{p}_g^*$, i.e., the 3-D coordinates in the optics frame $(xyz)_o$ of these image pixels.

Let $^i\mathbf{p} \in \mathbb{R}^3$ be the homogeneous coordinates of a relevant 2-D pixel point and $^w\mathbf{p} = [x_w, y_w, z_w, 1]^{\mathsf{T}}$ its corresponding unknown 3-D point expressed homogeneous coordinates. According to the pinhole camera model [35], these two points satisfy the following relation:

$$^i\mathbf{p}s = \mathbf{A}\begin{bmatrix} \mathbf{r}_1 & \mathbf{r}_2 & \mathbf{r}_3 & \mathbf{t} \end{bmatrix}{}^w\mathbf{p} \tag{7}$$

with $s \neq 0$ as a scaling factor, $\mathbf{A} \in \mathbb{R}^{3 \times 3}$ as the intrinsic parameter's matrix, and $\mathbf{T}_{c1}^w = [\mathbf{r}_1, \mathbf{r}_2, \mathbf{r}_3, \mathbf{t}] \in \mathbb{R}^{3 \times 4}$ as the extrinsic parameter's matrix [36]. Since the projected points are in the same plane (i.e., the ground plane), $^i\mathbf{p}$ and $^w\mathbf{p}$ satisfy the following homography transformation:

$$\begin{bmatrix} x_w & y_w & 1 \end{bmatrix}^{\mathsf{T}} = \left(\mathbf{A}\begin{bmatrix} \mathbf{r}_1 & \mathbf{r}_2 & \mathbf{t} \end{bmatrix}\right)^{-1}{}^i\mathbf{p}s. \tag{8}$$

In this way, we can compute $^o\mathbf{p}_{\text{img}}$, the corresponding point of an image pixel $^i\mathbf{p}$ under the optics frame via

$$^o\mathbf{p}_{\text{img}} = \mathbf{T}_l^o \mathbf{T}_{c1}^l \mathbf{T}_w^{c1} \begin{bmatrix} x_w & y_w & 0 & 1 \end{bmatrix}^{\mathsf{T}}. \tag{9}$$

Once the image pixel has been transformed to the frame $(xyz)_o$, we can formulate a simulation-based servoing problem to estimate the unknown solar orientation. For that, we select the outermost boundary as a representative image contour. We denote the center of this ellipse on the ground plane by $^o\mathbf{c}_{\text{img}} = [x_c, y_c]^{\mathsf{T}}$, from which the feature vector $\mathbf{y} \in \mathbb{R}^2$ of polar coordinates is computed as

$$\mathbf{y} = \begin{bmatrix} \Pi & \Theta \end{bmatrix}^{\mathsf{T}} = \begin{bmatrix} (x_c^2 + y_c^2)^{\frac{1}{2}} & \arctan(y_c/x_c) \end{bmatrix}^{\mathsf{T}}. \tag{10}$$

The construction of $\mathbf{y}$ is based on empirical observations of the ray-tracing model. In its general form, the elements of $\mathbf{y}$ are coupled with solar polar angle φ_0 and solar azimuthal angle θ_0 such that $\mathbf{y} = \mathbf{y}(\Pi(\varphi_0, \theta_0), \Theta(\varphi_0, \theta_0))$. When the lens plane is parallel to the ground plane, the variation of φ_0 affects the distance Π, and the variation of θ_0 affects the angle Θ (see Fig. 6), such that $\mathbf{y} = \mathbf{y}(\Pi(\varphi_0), \Theta(\theta_0))$.

The estimation of the solar orientation computed at the time step t is denoted by the vector $\boldsymbol{\vartheta}^t = [\varphi_0^t, \theta_0^t]^{\mathsf{T}}$, and its corresponding feature vector by $\mathbf{y}^t = [\Pi^t, \Theta^t]^{\mathsf{T}}$. These
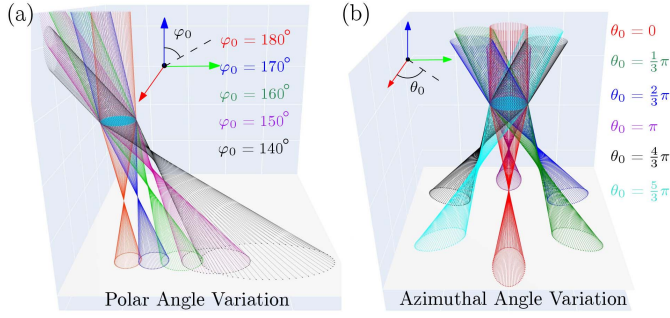
Fig. 6. Effect of the solar orientation variation on the light spot when the lens plane is parallel to the ground plane. (a) Effect of the variation of the solar polar angle φ_0. (b) Effect of the variation of the solar azimuthal angle θ_0.

two structures satisfy $\mathbf{y}^t = \mathbf{y}^t(\boldsymbol{\vartheta}^t)$. To differentiate the feature vector computed from image feedback with the feature vector computed from simulation, we denote the former by $\mathbf{y}_{\text{img}}$ and the latter by $\mathbf{y}^t$. Our method estimates the solar orientation by iteratively minimizing the difference between $\mathbf{y}^t$ and the feature $\mathbf{y}_{\text{img}}$ computed from image measurements [using (10)] as follows:

$$\boldsymbol{\vartheta}^{t+1} = \boldsymbol{\vartheta}^t - \lambda \mathbf{A}_t^{-1}(\mathbf{y}^t - \mathbf{y}_{\text{img}}) \tag{11}$$

where $\lambda > 0$ is a gain and $\mathbf{A}_t \in \mathbb{R}^{2\times 2}$ is the interaction matrix of the differential relation $(d/dt)\mathbf{y}^t = \mathbf{A}^t(d/dt)\boldsymbol{\vartheta}^t$ and is numerically computed with the ray-tracing model as follows:

$$\mathbf{A}_t = \begin{bmatrix} \dfrac{\Pi^t\left(\varphi_0^t + \delta, \theta_0^t\right) - \Pi^t}{\delta} & \dfrac{\Pi^t\left(\varphi_0^t, \theta_0^t + \delta\right) - \Pi^t}{\delta} \\ \dfrac{\Theta^t\left(\varphi_0^t + \delta, \theta_0^t\right) - \Theta^t}{\delta} & \dfrac{\Theta^t\left(\varphi_0^t, \theta_0^t + \delta\right) - \Theta^t}{\delta} \end{bmatrix} \tag{12}$$

for $\delta > 0$ as a small constant. The interaction matrix can be further simplified, e.g., if the RGB image is acquired when the lens surface is parallel to the ground plane, the variation of θ_0^t has no effect on Π^t, and the variation of θ_0^t has no effect on Θ^t, thus, $\mathbf{A}_t$ is diagonal. Also, note that we should set an initial guess for $\varphi_0^t \neq 0$, to avoid singularities of $\mathbf{A}_t$ at start. The estimation algorithm terminates when $\|\mathbf{y}^t - \mathbf{y}_{\text{img}}\|$ is smaller than the predefined value. The final estimation at the time instance t_f of the solar angles is denoted by $\widehat{\boldsymbol{\vartheta}} = [\widehat{\varphi}_0, \widehat{\theta}_0]^\mathsf{T} = \boldsymbol{\vartheta}^{t_f}$.

The selection of the geometric features for solar orientation estimation is not unique. There are other possible alternatives, e.g., the orientation or the shape of the ellipse. Since the solar orientation is parameterized by two variables, utilizing two features for estimation is sufficient. One requirement of the selected features is to be independent, to avoid $\mathbf{A}_t$ from becoming singular. The selected features should also be robust enough so that the estimation is reliable even in the presence of noise and inaccuracies, as we will discuss in Section V-B. We select features Π and Θ for our algorithm based on the aforementioned criteria.

An alternative approach is to compute and store the discrete mappings between the lens configuration and the geometric features, which computes the solar orientation estimation faster than the proposed interaction matrix-based method. In this

article, we utilize the interaction matrix-based techniques on account of its following merits: 1) it can save computer memory as the static mapping rule could require a large number of data stored for access during the operation and 2) it is more robust to the variation of the system settings. For example, if the optical or geometric parameters of the Fresnel lens are changed, the static mapping rule method requires a full recomputation, while the interaction matrix-based strategy can be applied directly.

IV. MOTION CONTROL ALGORITHMS

A. Lens Configuration Control

In this section, we derive a method to control the focus of solar rays over the target point $^{w}\mathbf{p}_i^*$. To this end, we model the solar energy power incident on the lens surface as

$$w_l = q_s \int_{A_l} \cos\beta \, \mathrm{d}A_l \tag{13}$$

where q_s is the solar irradiance (power per unit area), A_l is the area of the lens surface, and β is the angle between the Sun ray and the lens surface normal. Note that as the lens is flat, β remains constant for every $\mathrm{d}A_l$. To maximize the solar energy power incident to the lens, the lens surface normal should be aligned with the estimated orientation of the incident sunlight.

The estimated solar orientation in the robot frame $(xyz)_r$ is calculated as $^{r}\widehat{\mathbf{s}}_0 = \mathbf{T}_l^r \mathbf{T}_o^l{}^{o}\widehat{\mathbf{s}}_0$, where $^{o}\widehat{\mathbf{s}}_0$ is the estimated solar orientation computed by substituting $\widehat{\boldsymbol{\vartheta}}$ into (2). The target point $^{w}\mathbf{p}_i^*$ is the location on the ground where the concentrated light spot needs to be placed, which is shown in Fig. 3. It can be transformed into the robot frame $(xyz)_r$ as $^{r}\mathbf{p}_i^* = \mathbf{T}_l^r \mathbf{l}_{c_1}^r \mathbf{T}_w^{c_1}{}^{w}\mathbf{p}_i^*$. The target lens position in the robot frame $(xyz)_r$ is then computed as

$$^{r}\mathbf{p}_l^* = {}^{r}\mathbf{p}_i^* - d_{\text{lp}}{}^{r}\widehat{\mathbf{s}}_0 \tag{14}$$

where d_{lp} is the distance between the lens center and the target point. Equation (15) describes how to align the orientation of the lens toward the estimated solar orientation $^{r}\widehat{\mathbf{s}}_0$, which is expressed in zyx Tait–Bryan angles $\alpha_l^*, \beta_l^*, 0$

$$\begin{bmatrix} -\mathrm{C}\alpha_l^*\mathrm{S}\beta_l^* & -\mathrm{S}\alpha_l^*\mathrm{S}\beta_l^* & \mathrm{C}\beta_l^* & 0 \end{bmatrix}^\mathsf{T} = -{}^{r}\widehat{\mathbf{s}}_0. \tag{15}$$

The target lens pose is constructed as $\Omega^* = [{}^{r}\mathbf{p}_l^{*\mathsf{T}}, \alpha_l^*, \beta_l^*, 0]^\mathsf{T}$. By using the robot's inverse kinematics, we can then transform the target pose Ω^* into its corresponding target joint configuration $\mathbf{x}^*$, which is then sent to the robot's control system to command the motion.

Fig. 7 shows the effect of varying the lens configuration on the concentration of Sun rays. This visualization is divided into various sequential processes, i.e., the alignment of the polar angle, the alignment of the azimuth angle, and the translation of the lens to $^{r}\mathbf{p}_l^*$. This figure shows that by first orienting the lens parallel to the ground and then translating it toward the incident point, the collected solar power and the lens' optical concentration can both be optimized. This strategy is adopted by our proposed motion controller.

Nevertheless, we argue that it is not strictly required to include the reorientation process for all robot solar concentration tasks. As shown in Fig. 7(b), the lens is capable (to some
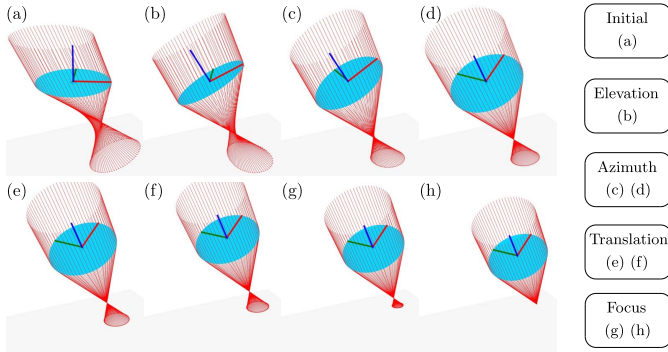
Fig. 7. Simulations of the process of lens reorientation and focus, with polar angle $\varphi_0 = 5/6\pi$ and azimuthal angle $\theta_0 = 1/6\pi$. (a) Initial lens configuration. (b) Align elevation angle. (c) and (d) Align azimuthal angle. (e) and (f) Lens translation. (g) and (h) Focus.

extent) of concentrating solar energy even if the lens is not perfectly parallel to the ground. When the robot's DOF is limited, it is still possible to achieve suboptimal solar concentration. Moreover, from Fig. 6(a), we can see that the distance between the lens and the optimal focal point decreases, while the angular offset between lens surface normal and solar elevation increases. This unique optical characteristic could be exploited by robots with limited manipulability.

B. Parameter Selection for Motion Control

In this section, we analyze the heat transfer process involved before, during, and after wood pyrolysis. Then, we design a series of experiments, to identify the motion control parameters, specifically, the desired lens configuration and the termination criteria for the solar pyrolysis process.

1) Prepyrolysis Stage: Wood pyrolysis is a chemical reaction that is triggered when the wood temperature T_w reaches the pyrolysis point T_p. Depending on the type of wood, T_p varies from 200 °C to 400 °C. During the heating process, if $T_w < T_p$, the external heat inflow mainly induces physical changes, including the vaporization of the volatiles and the increment of the wood's temperature T_w. According to the heat transfer principles, if the external heat flux q_e (power per unit area) is not strong enough, T_w will only reach a steady-state temperature $T_w = T_{ss} < T_p$, but no charred regions will be produced. To actually trigger the desired reaction at the target point, q_c should be maintained above a target threshold q_c^*. In our study, the relationship between q_c and the robot joint configuration $\mathbf{x}$ is modeled as

$$q_c = \alpha \kappa q_s A_l / A_c(\mathbf{x}) \tag{16}$$

where $\alpha \in (0, 1)$ denotes the absorptance of the ground plane, $\kappa \in (0, 1)$ is a factor quantifying the solar energy loss due to lens absorption, A_l is the lens surface area, A_c is the concentrated solar spot area, and $A_c(\mathbf{x})$ is the function mapping the robot joint configuration $\mathbf{x}$ to A_c. Since the lens configuration is always aligned with the solar orientation, we can vary q_c by changing d_{lp} (i.e., the distance between lens center and target point) so that $A_c(\mathbf{x}) \equiv A_c(d_{\mathrm{lp}})$. The mapping function $A_c(d_{\mathrm{lp}})$ is calculated with our proposed ray-tracing simulation model.

However, note that it is difficult to accurately obtain the true parameters $\alpha, \kappa, q_s, q_c^*$. To deal with this issue, instead
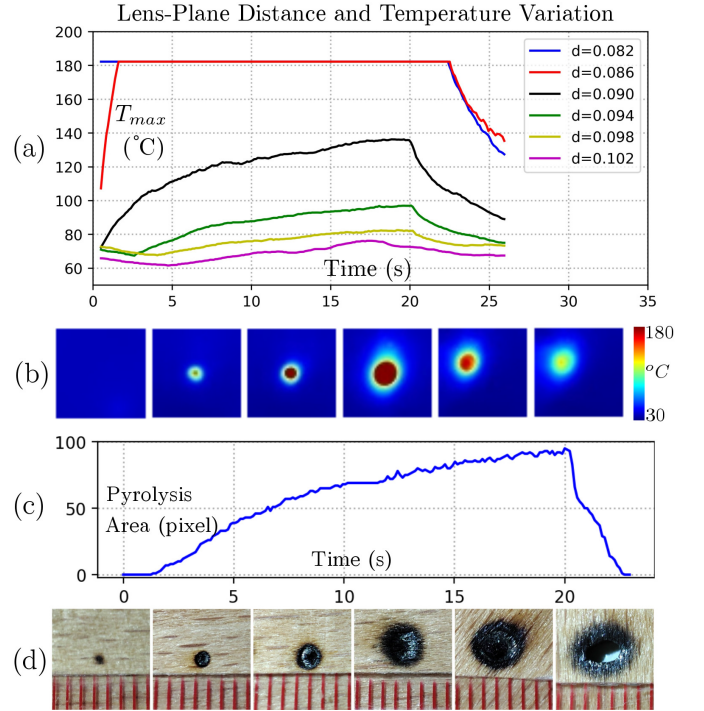

Fig. 8. Experiments designed to determine the parameters for the motion control algorithm. (a) Solar concentration experiments with fixed duration and varying lens-to-plane distance. (b) Representative thermal images captured before, during, and after the wood pyrolysis process. (c) Variation of the pyrolysis region with respect to time when the lens-to-plane distance is set to 0.086 m. (d) Size of a carbonized point can be controlled by the selection of $\overline{N_p}$.

of relying on adaptive temperature control [21] or a precise thermal dynamics model, we implement a simple yet effective solution where we set $d_{\mathrm{lp}} = \overline{d_{\mathrm{lp}}}$, for $\overline{d_{\mathrm{lp}}}$ as an empirical value, based on collected experimental data. To this end, we conduct a series of experiments with varying d_{lp} and a fixed heating duration of around 20 s. With our tests, we found that the target point is carbonized when d_{lp} is set to 8.2 cm and 8.6 cm, which is close to the focal length indicated by the manufacturer (8.0 cm). To terminate the heating process, we set $d_{\mathrm{lp}} = \overline{d_{\mathrm{lp}}} + \delta_{d_{\mathrm{lp}}}$ where the offset is set to $\delta_{d_{\mathrm{lp}}} = 3$ cm. The temperature profile at the target point is monitored with the thermal camera, and its maximum value at time instant t is denoted by T_t^{max}. Fig. 8(a) shows the temporal evolution of this variable. Note that in these tests, T_t^{max} is capped at $T_c^{\mathrm{max}} = 180.9$ °C, which is the hardware upper limit of our thermal camera. Since T_c^{max} is close to the theoretical range of wood pyrolysis temperature, we can fairly assume that $T_c^{\mathrm{max}} = T_p$ to compensate for the hardware's limitations.

2) Pyrolysis Stage: Once pyrolysis has been triggered, the wood components (e.g., cellulose) start to react with oxygen to produce water, carbon dioxide, and charred spots. Afterward, if q_c is continuously applied, the pyrolysis region starts to expand over the surface due to the exothermic chain reaction and propagation of vaporization. In Fig. 8(b), we depict successive thermal images collected during the tests with $d_{\mathrm{lp}} = 8.6$ cm. We find that the temperature of the target point's center region increases faster than its surrounding, and it is the first to reach T_p. We denote by N_p the number of pixels

having reached T_p in a thermal image and depict the temporal evolution of this area for $d_{lp} = 8.6$ cm in Fig. 8(c). We choose N_p as a proxy of the actual carbonized area of the target point.

As shown in Fig. 8(a), it is more time-efficient to create a relatively small carbonized area by setting $\overline{d_{lp}} = 8.2$ cm and than by setting it to $\overline{d_{lp}} = 8.6$ cm. To create a series of carbonized points of uniform size, in the motion control algorithm, we set $N_p \geq \overline{N_p}$ as the termination criteria for the solar concentration method. Our tests reveal that setting $\overline{N_p} = 30$ will produce a carbonized point with a diameter of around 0.2 cm.

3) Postpyrolysis Stage: In this study, the surface area of the Fresnel lens is relatively small, and therefore, the concentrated solar energy inflow is not strong enough to trigger a spontaneous exothermic process (i.e., the continuous burning of the wood). Thus, when the process of the solar concentration is terminated by the robot motion, the temperature of the target point should drop immediately. However, we find that for tests where $d_{lp} = 8.2$ cm and $d_{lp} = 8.6$ cm, T_t^{max} remains at a constant high value for around 3 s after the solar concentration is terminated. This is mainly due to the actual pyrolysis temperature being higher than the camera's upper limit T_c^{max}, as it takes time for T_w to drop to T_c^{max}. Afterward, the actual variation of T_w can be captured by the thermal camera. This phenomenon is worth mentioning since we are using N_p as the termination criterion of the heating controller. In such a case, if we start to heat the next target point immediately after the condition $N_p \geq \overline{N_p}$ is fulfilled, the high-temperature region of the previous target point will also be counted in the current calculation of N_p. To solve this problem, we programmed the robot to not proceed to heat the next target point until N_p has dropped to null.

C. Heliography Path Generator

The aim of the developed robotic system is to create uniform carbonized black points at a group of target positions P_w on the ground plane. To this end, the first step is to transform the target image into a binary image I_b. Since the resolution of I_b depends on I_t, if each pixel with a positive value in I_b is mapped to P_w, the operation time of a solar painting task will be very long, and some target positions might be out of the robot's working range. Moreover, since the solar energy is concentrated at the area of interest A_c, we require an algorithm for avoiding overlapping elements in P_w. To solve the aforementioned problems, feature extraction and scaling operations are applied to I_B to generate a low-resolution feature image I_f.

Feature extraction techniques are applied depending on the characteristics of I_t. For monochrome target images including text, logos, and symbols as in Fig. 9(a$_1$), (b$_1$), and (c$_1$), we use the Canny edge detector from the OpenCV library [37] to extract the contours in the image as a representative feature. Note that in Fig. 9(c$_1$), a part of the trace is so narrow that it may cause path overlapping. Therefore, we use the centerline of the closed contour as a desired feature. For target images that contain abundant color information such as the humanoid portrait shown in Fig. 9(d$_1$), the pattern of the images cannot be well represented by edges. In this
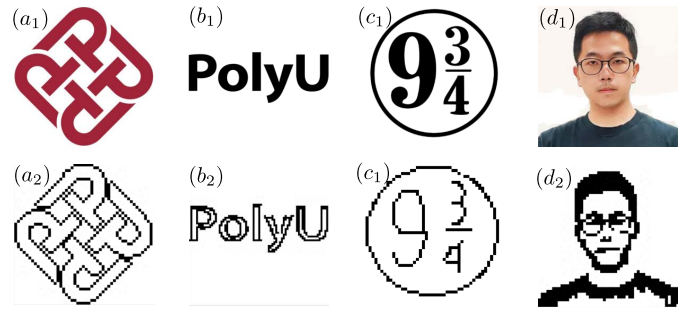

Fig. 9. Feature extraction and scaling from target figures for path planning. The obtained target points were used for conducting real solar painting experiments as reported in Section V-C. (a) Example of logo. (b) Example of text. (c) Example of image pattern. (d) Example of human portrait.

case, we use the adaptive threshold function and a series of denoising filters implemented in OpenCV to generate I_b.

Now, we introduce the method for scaling and mapping the image pixels to the pattern's points. Consider the binary image I_b of dimensions $x_b \times y_b$ (pixels). We define the working canvas on the ground plane as a square region of dimensions $l_w \times l_w$ cm. The scaling factor is computed as

$$\omega_s = l_w / (\max(x_b, y_b) \cdot r_p) \qquad (17)$$

where r_p is the radius of the projected light spot. As mentioned in Section IV-B, the parameter of the motion controller is set to $\overline{N_p} = 30$, which will produce a carbonized point with a diameter of around 0.2 cm. Thus, we set $r_p = 0.2$ cm to compute the scaling factor ω_s. For each image pixel (u, v) from I_b, its corresponding target position on the ground plane is computed as ${}^w\mathbf{p}_i^* = [u r_p + d_x, v\ r_p + d_y, 0, 1]^\mathsf{T}$, where (d_x, d_y) defines the displacement from the origin (the center of the ArUco marker). These computed world coordinates are then grouped according to u, ordered according to v, and stored in an ordered list P_w, which is then sent to the motion controller described in Algorithm 1. In the experiments, we set $d_x = d_y = 5$ cm to avoid burning the ArUco marker. The l_w term determines the actual size of the solar painting. We select this parameter based on the constraint $l_w < 10$ cm such that the target configurations of the robot arm stay within its working range.

Recall that in Section III-C, the solar orientation with respect to the robot frame is estimated and denoted by $\widehat{\boldsymbol{\vartheta}}$. As the actual solar configuration varies with time during a solar painting process, $\widehat{\boldsymbol{\vartheta}}$ should be updated accordingly. In our method, instead of solving the simulation-based servoing problem again (as it requires additional computational time), we update $\widehat{\boldsymbol{\vartheta}}$ by adding a time-varying correction factor. To this end, let us denote the conventional solar orientation (i.e., the azimuthal/elevation angles with respect to North/horizon) at the time instant t by $\boldsymbol{\vartheta}_c^t$. Given the latitude and longitude information, $\boldsymbol{\vartheta}_c^t$ can be obtained from the Python library Pysolar [38]. At the system calibration stage, the initial conventional solar orientation is recorded as $\boldsymbol{\vartheta}_c^{t_0}$. Accordingly, the solar orientation with respect to the robot frame at time instant t and the orientation $\widehat{\boldsymbol{\vartheta}}$ can be updated as

$$\widehat{\boldsymbol{\vartheta}}^t = \widehat{\boldsymbol{\vartheta}} + \left(\boldsymbol{\vartheta}_c^t - \boldsymbol{\vartheta}_c^{t_0}\right) \qquad (18)$$

Algorithm 1 Motion Control of the Robot Given P_w

---

1 Robot-World Calibration ← Section II-B;
2 Initial Solar Orientation Estimation $\widehat{\boldsymbol{\vartheta}}$ ← Section III-C;
3 Target Position List ← $P_w = \{^w\mathbf{p}_1^*, \ldots, {}^w\mathbf{p}_k^*\}$;
4 Target Position Index $i \leftarrow 1$;
5 **while** $i \leq k$ **do**
6   **while** $N_p \leq \overline{N_p}$ **do**
7       $N_p \leftarrow$ Thermal Camera; $d_{lp} = \overline{d_{lp}}$;
8       ${}^r\mathbf{p}_l^* \leftarrow$ (14);
9   **end**
10   **while** $N_p \geq 0$ **do**
11      $N_p \leftarrow$ Thermal Camera; $d_{lp} \leftarrow \overline{d_{lp}} + \delta_{d_{lp}}$;
12      ${}^r\mathbf{p}_l^* \leftarrow$ (14);
13   **end**
14   $i \leftarrow i + 1$; Update $\widehat{\boldsymbol{\vartheta}}^t \leftarrow$ (18);
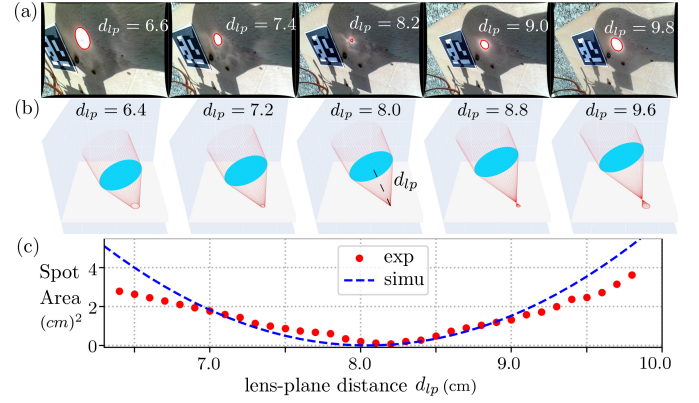15 **end**

Fig. 10. Image-based focal length calibration experiment. (a) Snapshots of captured light spot and extracted contour. (b) Corresponding lens-to-plane configuration in the developed simulation. (c) Comparison between the light spot area from the real images and the simulation.

where the term $\boldsymbol{\vartheta}_c^t - \boldsymbol{\vartheta}_c^{t0}$ effectively acts as the time-varying correction factor. Note that when the the additional geometrical and temporal information is not available, the correction factor cannot be computed directly. However, the solar orientation can still be updated by capturing new images of the solar spot and conducting the proposed image-based estimation algorithm accordingly.

V. RESULTS

A. Focal Length Calibration

In this section, we compare the results of A_c computed from simulation with those from the sensor feedback. To conduct the validation, we first align the orientation of the lens with the estimated Sun orientation and, then, control the robot to focus the Sun on a target point with varying lens-to-plane distance d_{lp} from 6.4 to 9.8 cm, with a uniform step of 0.1 cm. As shown in Fig. 10(a), the contour of the projected light spot is extracted and depicted in red. The image pixels of the solar spot are then transformed into 3-D coordinates in $(xyz)_r$ coordinates, and the actual area of the solar spot is computed accordingly. Note that this step is necessary since the position of the camera is also moving with respect to the ground plane, making the direct correlation between the amount of pixels of interest in the image and the actual solar spot size ambiguous.

The relationship between the actual A_c computed from experiments and the lens-to-plane distance d_{lp} is shown in Fig. 10(c) with red dots. The theoretical values of A_c under the same solar orientation and lens configuration are obtained through the simulation and shown in Fig. 10(c), with the blue dashed line. We find that the coupling between A_c and d_{lp} is similar in the experiment and the simulation, and the value of d_{lp} that corresponds to the minimum A_c in the experiment is 8.2 cm, which is close to the focal length $f_l = 8.0$ cm provided by the manufacturer. The match between theory and practice demonstrates the effectiveness of the proposed sensor-based calibration method. Nevertheless, obtaining A_c from real-time sensor feedback is a challenging task from an image processing perspective. As shown in Fig. 10, there may

exist regions of the image (e.g., the white region of the ArUco marker) with similar brightness as the concentrated light spot. In our case, the region of interest that contains the light spot is manually selected.

B. Solar Orientation Estimation Experiments

We conducted four experiments denoted by $E_{i=1,2,3,4}$. In each experiment, the orientation of the robot is arbitrarily set. The lens plane is set to be parallel to the ground plane and the lens yaw angle is set to vary within a range $\beta_l^* \in [-B^i, B^i]$ with a step of 0.5 °C, where $B^1 = B^3 = 25$ °C, $B^2 = 35$ °C, and $B^4 = 15$ °C, while the lens center $\mathbf{O}_l$ is maintained at a constant position. In these estimation experiments, we collected around 400 RGB images of the light spot. The kth captured image in the E_i experiment is denoted by I_k^i, and the corresponding robot configuration $\mathbf{x}_k^i$ is also recorded. Some representative images $I_k^{i=1,2,3,4}$ are shown in Fig. 11(a₁)–(a₄), respectively, and the corresponding robot configurations are visualized in Fig. 11(c₁)–(c₄), respectively. Fig. 11(b) provides the annotations of the robot configuration in these tests. The term "original end-effector" refers to the tool center point of the robot arm where the motorized lens system is added, which is denoted as $\mathbf{O}_{oe}$ in Fig. 3.

In Fig. 11(b) and (c₁)–(c₄), the red ellipse representing the light spot is generated by mapping the contour of interest in I_i^k to the robot frame $(xyz)_r$. The (position-based) geometric feature vector $\mathbf{y}$ of the red ellipse, which is defined in (10), is used to estimate the solar azimuthal angle θ_0 and the solar elevation angle φ_0.[3] To quantitatively evaluate the performance of the solar orientation estimation method, we denote the mean and variance of the solar azimuthal angle estimation by utilizing the feature $\mathbf{y}$ by μ_{a_p} and σ_{a_p}. We denote the mean, variance, and mean error of the solar elevation angle estimation utilizing features $\mathbf{y}$ by μ_{e_p}, σ_{e_p}, and e_{e_p}. The calculated results of the four experiments are reported in Fig. 12(a), where we find that variances σ_{a_p} and σ_{e_p} in all experiments have

---

[3]The feature vector $\mathbf{y}$ is actually defined in frame $(xyz)_o$. As the transformation between $(xyz)_o$ and $(xyz)_r$ is known, $\mathbf{y}$ can be easily computed from the red ellipse in $(xyz)_r$.
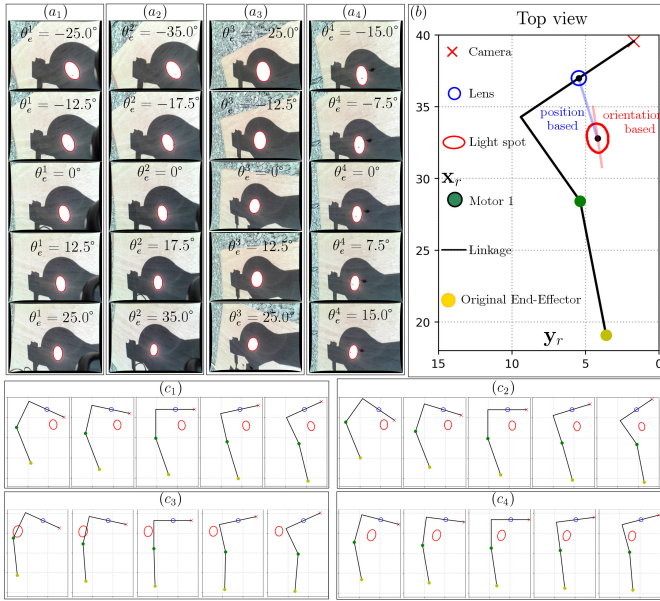
Fig. 11. Experiments evaluating the performance of the solar orientation estimation utilizing different geometric features. (a_1)–(a_4) Images captured from four experiments with varying lens yaw angles. (c_1)–(c_4) Corresponding robot configuration from the top view. (b) Components in the robot configuration visualization.
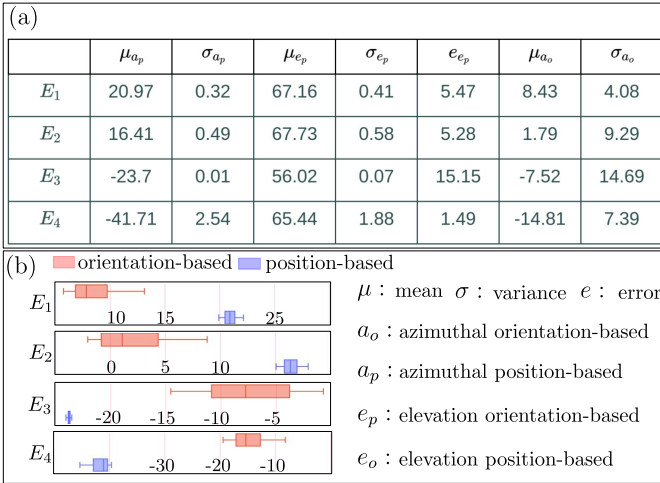

Fig. 12. (a) Quantitative evaluation of the performance of different estimation methods. (b) Position-based method outperforms the orientation-based method, in terms of accuracy and stability.

relatively low values (less than 3 °C), which corresponds to the practical conditions of experiment E_i. Observing the mean error term e_{e_p}, we find that the mean error values of E_1, E_2, and E_4 are acceptable, while the error value of E_3 is relative large.[4] We claim that such undesirable estimation error occurs in practice since the proposed estimation method purely relies on image feedback for obtaining transformation matrices, which can be sometimes inaccurate. Such error can be reduced

---

[4]The error between the estimated and real solar elevation angle can be obtained since the robot and the ground plane are all placed on the ground. Yet, the real value of the robot's orientation with respect to north is unknown since there is no external device integrated with the system. Thus, we use the variance as an alternative to evaluate the estimation of solar azimuthal angle.
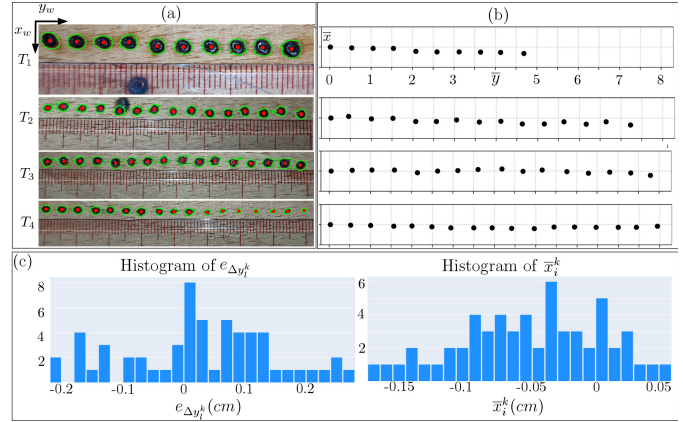

Fig. 13. Validation of the positional accuracy of the developed system. The mean of the horizontal error is 0.099 cm, and the mean of vertical error is 0.061 cm. (a) Solar concentration point positioning based on image processing. (b) Depiction of the extracted feature points. (c) Quantitative evaluation and visualization of the accuracy.

if more sensors, e.g., compass and IMU, are integrated in the system.

Besides the position-based feature vector $\mathbf{y}$, there are other types of sensor-based geometric features, which can be used for solar orientation estimation. For example, when the lens plane is set parallel to the ground plane, the orientation of the principal axis of the ellipse [denoted by "orientation-based" feature in Fig. 11(b)] is coupled with the solar azimuthal angle, and the eccentricity (shape) of the ellipse is coupled with the solar elevation angle. The two geometric features for solar orientation estimation can be selected arbitrarily as long as they are not linearly dependent. Yet, we find that the orientation and shape features of the light spot are more sensitive to inaccurate system calibration compared to the position-based features. For example, we denote the variance of the solar azimuthal angle estimation using the orientation-based feature by σ_{a_o}. The comparison between σ_{a_o} and σ_{a_p} is shown in Fig. 12(b). The position-based feature that yields more stable estimations is finally selected for the proposed method.

C. Robotic Solar Painting Experiments

We conducted four tests to evaluate the proposed system's accuracy of focusing solar energy on the given target positions. We denote the four tests by $T_{i=1,2,3,4}$, and the kth target point in T_i is denoted by ${}^{w}\mathbf{p}_i^k = [x_i^k, y_i^k]^\mathsf{T}$. For each test, we set x_i^k to a constant value, while $y_i^{k+1} = y_i^k + \Delta y$, where $\Delta y = 0.5$ cm is a constant adjacent distance. The results of the four tests are shown in Fig. 13(a), and a desk ruler is used as a reference for position measurement. The contours of the carbonized points in the images are extracted, and the image coordinates of each contour are recorded. The mapping ratio between the image pixel values and an actual metric distance is obtained by manually calculating the pixel value difference of a fixed distance indicated by the desk ruler. The metric positions of the carbonized points in each test are denoted by ${}^{w}\overline{\mathbf{p}}_i^k = \begin{bmatrix} \overline{x}_i^k & \overline{y}_i^k \end{bmatrix}^\mathsf{T}$ and shown in Fig. 13(b), where $\overline{x}_i^0$ is set to zero as a reference value. We define the actual adjacent distance between two points as $\Delta\overline{y}_i^k = \overline{y}_i^{k+1} - \overline{y}_i^k$, and the error of $\Delta\overline{y}_i^k$ is calculated as $e_{\Delta y_i^k} = \Delta y - \Delta\overline{y}_i^k$. To quantitatively

Fig. 14.   Results of the solar painting experiments. The robot path is planned according to the feature points extracted from the target pattern.

analyze the accuracy, we calculate the mean of $|e_{\Delta y_i^k}|$ as $\mu_{\Delta y} = 0.099$ cm and the mean of $|\overline{x}_i^k|$ as $\mu_{\overline{x}} = 0.061$ cm, and the corresponding histograms are shown in Fig. 13(c). In general, the accuracy performance of the developed system is sufficient for conducting solar painting tasks.

We conducted solar painting experiments with various target patterns and different scaling factors to validate the proposed methods. The process and results of four representative experiments are shown in Fig. 14. Depending on the amount of target positions sent to the robot's motion controller, the operation time for each heliography experiment varies from 7 to 15 min. One complication of the proposed robotic approach comes from the difficulty to accurately detect the ground plane. In our method, we assume that the ground is flat such that the homography transformation is valid and can be determined by an ArUco marker. However, as the wooden surface may (slightly) deform after being exposed to solar energy for a long period, this constraint may not be exactly satisfied. Also, note that as many commercial depth cameras rely on infrared light, thus, they may perform poorly in outdoor environments. Another limitation of the proposed method is the difficulty to observe the point where solar energy is concentrated. One possible solution is to calibrate the thermal camera [39] that is invariant to light intensity for determining the location of this point. To ensure the tracking of the solar concentration spot in the presence of environmental noise, learning-based approaches for robust image segmentation could be implemented [40].

The accompanying video demonstrates the performance of the proposed robotic heliography system with multiple experiments: https://github.com/JinliBot7/SR/raw/main/video.mp4

In terms of accuracy and time efficiency, utilizing a laser engraving machine could produce similar or even better results as in Fig. 14. Yet, we would like to emphasize the following merits of the proposed sensor-based solar painting robotic system. The core component for solar energy concentration

is a plastic Fresnel lens. Compared to a laser generator, the lightweight Fresnel lens is more compatible with a robotic arm that has a limited payload. The solar energy is exploited directly without utilizing any additional devices such as solar cells or batteries. Such compact design makes the system specifically suitable for field robotics applications and also saves the cost. Moreover, we hope that the novel combination of robotics, art, and renewable energy is attractive and will arise people's attention on the urgent topic of environment protection.

VI. Conclusion

In this article, we presented a novel sensor-based robotic system that is capable of automatically performing heliography, an art form that involves the creation of pictorial patterns on a wooden canvas by concentrating solar energy over it. In order to focus on the Sun rays, the robot's end-effector rigidly grasps a Fresnel lens and is equipped with thermal and RGB cameras. To perform the procedure, a desired input figure is analyzed to extract contour features, which results in a series of target points where solar energy will be concentrated. Then, the motion controller calculates the required robot position such that solar energy is concentrated over each of these points. The Sun direction is estimated in real time based on visual feedback to maximize the Sun rays passing through the lens. To create carbonized points of uniform size, our sensor-based method monitors the wood pyrolysis and thus calibrates the focal distance to the surface.

As a preliminary step toward robotic painting by harnessing solar energy, our work has achieved promising results. Specifically, we identify that the key to the success of the experiments lies in the accurate estimation of the Sun direction, as well as on proper determination of the lens-to-plane distance. To estimate the Sun direction, we design an iterative update rule that is based on the interaction (Jacobian) matrix of the system, which captures the relationship between the Sun angle increments and the feature variations. We select a position-based feature vector over an orientation-based feature since it exhibits smaller variance and thus leads to more accurate and stable estimation. The effectiveness of our innovative heliography system is verified by autonomously drawing various representative patterns, namely, a university logo, letters, a human portrait, and numbers.

There are certainly a few limitations associated with our current approach. For example, our system cannot function well during cloudy or rainy days, although this issue is also encountered by other solar energy-dependent applications [41]. When the sunlight is completely blocked by clouds, the temperature will not rise to the critical point and the robot will wait at a target position until the sunlight reappears. When the Sun is partially blocked, pyrolysis cannot be reached in a consistent manner [see Fig. 15(d)]. On the other hand, working for a long period under intensive sunlight could also cause problems since overheating the motors and other electrical components might bring potential risks to the robot. Since adding a heat shield might hinder robot motion, the current solution is to manually place the main body of the system under the shadow and only expose to sunlight the end-effector part which carries
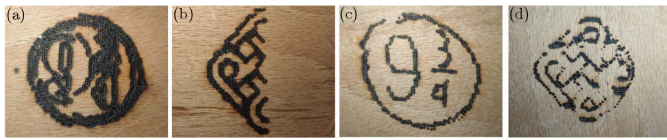
Fig. 15. Examples of failed solar paintings, which are caused by (a) inappropriate feature selection in the path planning stage, (b) lens being shadowed as the solar orientation changed, (c) inaccurate solar orientation estimation, and (d) cloudy situation when N_p is set too small.

the lens. Yet, the position of the shadow moves as time passes, so it may cover the end-effector after a period of time, causing the termination of an ongoing task. Besides, since our robotic prototype is a fixed-base manipulator, the limited workspace of the robot end-effector limits the size of the heliographic painting.

For future work, there are several directions along which we are interested in investigating. A feasible solution to paint a large picture is to use a mobile/wheeled robot manipulator such that the painting range can be considerably extended [42]. For motion generation, it is worth investigating the transfer of drawing skills from a human teacher to a robot so that the procedure of image processing the desired pattern can be bypassed [43]. Besides, proper coordination between the end-effector and joint links would be necessary when the robot moves into a configuration where the links block the sunlight [44]. For the Sun angle estimation, we would like to integrate the recent advances in the determination of plane of array (POA) solar irradiation on inclined surfaces so that the optimal tilt and azimuth angles could be obtained to maximize the power output [45].

REFERENCES

[1] C. Kruse. (2018). *Sunlight Art: Painting With a Magnifying Glass*. [Online]. Available: https://www.ripleys.com/weird-news/sunlight-art/

[2] *Sunscribes*. Accessed: Aug. 8, 2022. [Online]. Available: https://www.sunscribessolarprinting.com/

[3] Y. Sun and Y. Xu, "A calligraphy robot—Callibot: Design, analysis and applications," in *Proc. IEEE Int. Conf. Robot. Biomimetics (ROBIO)*, Dec. 2013, pp. 185–190.

[4] S. Calinon, J. Epiney, and A. Billard, "A humanoid robot drawing human portraits," in *Proc. 5th IEEE-RAS Int. Conf. Hum. Robots*, Dec. 2005, pp. 161–166.

[5] R. Liu, W. Wan, K. Koyama, and K. Harada, "Robust robotic 3-D drawing using closed-loop planning and online picked pens," *IEEE Trans. Robot.*, vol. 38, no. 3, pp. 1773–1792, Jun. 2021.

[6] M. Muddassir, D. G. Dominguez, L. Hu, S. Chen, and D. Navarro-Alarcon, "Robotics meets cosmetic dermatology: Development of a novel vision-guided system for skin photo-rejuvenation," *IEEE/ASME Trans. Mechatronics*, vol. 27, no. 2, pp. 666–677, Apr. 2022.

[7] K. F. Tamrin, K. Moghadasi, M. H. Jalil, N. A. Sheikh, and S. Mohamaddan, "Laser discoloration in acrylic painting of visual art: Experiment and modeling," *Materials*, vol. 14, no. 8, p. 2009, Apr. 2021.

[8] P. Xyntarianos-Tsiropinas, K. Bailas, and T. Spyrou, "Photon painter: A robotic device that transfers drawings onto a large surface area using laser beam on photomechanical reaction materials," in *Proc. EVA London*, 2019, pp. 84–88.

[9] F. Yettou, B. Azoui, A. Malek, A. Gama, and N. L. Panwar, "Solar cooker realizations in actual use: An overview," *Renew. Sustain. Energy Rev.*, vol. 37, pp. 288–306, Sep. 2014.

[10] P. A. Plonski, P. Tokekar, and V. Isler, "Energy-efficient path planning for solar-powered mobile robots," *J. Field Robot.*, vol. 30, no. 4, pp. 583–601, 2013.

[11] S. Gorjian, S. Minaei, L. MalehMirchegini, M. Trommsdorff, and R. R. Shamshiri, "Applications of solar PV systems in agricultural automation and robotics," in *Photovoltaic Solar Energy Conversion*. Amsterdam, The Netherlands: Elsevier, 2020, pp. 191–235.

[12] Y. Chu, M. Li, and C. F. M. Coimbra, "Sun-tracking imaging system for intra-hour DNI forecasts," *Renew. Energy*, vol. 96, pp. 792–799, Oct. 2016.

[13] A. B. Afarulrazi, W. M. Utomo, K. L. Liew, and M. Zarafi, "Solar tracker robot using microcontroller," in *Proc. Int. Conf. Bus., Eng. Ind. Appl.*, Jun. 2011, pp. 47–50.

[14] Z. El Kadmiri, O. El Kadmiri, L. Masmoudi, and M. N. Bargach, "A novel solar tracker based on omnidirectional computer vision," *J. Sol. Energy*, vol. 2015, pp. 1–6, Jan. 2015.

[15] P. Arlikar, A. Bhowmik, M. Patil, and A. Deshpande, "Three dimensional solar tracker with unique sensor arrangement," in *Proc. Int. Conf. Smart Technol. Manage. Comput., Commun., Controls, Energy Mater. (ICSTM)*, May 2015, pp. 509–513.

[16] V. Peretroukhin, L. Clement, and J. Kelly, "Inferring Sun direction to improve visual odometry: A deep learning approach," *Int. J. Robot. Res.*, vol. 37, no. 9, pp. 996–1016, Aug. 2018.

[17] Y. Ma, X. Fan, J. Cai, J. Tao, Y. Gao, and Q. Yang, "Application of sensor data information cognitive computing algorithm in adaptive control of wheeled robot," *IEEE Sensors J.*, early access, Jan. 25, 2021, doi: 10.1109/JSEN.2021.3054058.

[18] E. Cippitelli, F. Fioranelli, E. Gambi, and S. Spinsante, "Radar and RGB-depth sensors for fall detection: A review," *IEEE Sensors J.*, vol. 17, no. 12, pp. 3585–3604, Jun. 2017.

[19] B. Lu *et al.*, "Toward image-guided automated suture grasping under complex environments: A learning-enabled and optimization-based holistic framework," *IEEE Trans. Autom. Sci. Eng.*, early access, Dec. 29, 2021, doi: 10.1109/TASE.2021.3136185.

[20] J. Shor, "Compact thermal sensors for dense CPU thermal monitoring and regulation: A review," *IEEE Sensors J.*, vol. 21, no. 11, pp. 12774–12788, Jun. 2020.

[21] L. Hu, D. Navarro-Alarcon, A. Cherubini, M. Li, and L. Li, "On radiation-based thermal servoing: New models, controls, and experiments," *IEEE Trans. Robot.*, vol. 38, no. 3, pp. 1945–1958, Jun. 2021.

[22] C. Zhong, W. W. Y. Ng, S. Zhang, C. D. Nugent, C. Shewell, and J. Medina-Quero, "Multi-occupancy fall detection using non-invasive thermal vision sensor," *IEEE Sensors J.*, vol. 21, no. 4, pp. 5377–5388, Feb. 2020.

[23] Y. Cao *et al.*, "Depth and thermal sensor fusion to enhance 3D thermographic reconstruction," *Opt. Exp.*, vol. 26, no. 7, pp. 8179–8193, 2018.

[24] G. B. Palmerini, "Combining thermal and visual imaging in spacecraft proximity operations," in *Proc. 13th Int. Conf. Control Autom. Robot. Vis. (ICARCV)*, Dec. 2014, pp. 383–388.

[25] A. Cherubini and D. Navarro-Alarcon, "Sensor-based control for collaborative robots: Fundamentals, challenges, and opportunities," *Frontiers Neurorobot.*, vol. 14, p. 113, Jan. 2021.

[26] A. Duan, M. Victorova, J. Zhao, Y. Sun, Y. Zheng, and D. Navarro-Alarcon, "Ultrasound-guided assistive robots for scoliosis assessment with optimization-based control and variable impedance," *IEEE Robot. Autom. Lett.*, vol. 7, no. 3, pp. 8106–8113, Jul. 2022.

[27] S. Huo *et al.*, "Keypoint-based planar bimanual shaping of deformable linear objects under environmental constraints with hierarchical action framework," *IEEE Robot. Autom. Lett.*, vol. 7, no. 2, pp. 5222–5229, Apr. 2021.

[28] J. Rath, M. Wolfinger, G. Steiner, G. Krammer, F. Barontini, and V. Cozzani, "Heat of wood pyrolysis," *Fuel*, vol. 82, no. 1, pp. 81–91, 2003.

[29] A. M. Andrew, "Multiple view geometry in computer vision," *Kybernetes*, vol. 30, pp. 1333–1341, Dec. 2001.

[30] P. D. Lin, *Advanced Geometrical Optics*. Singapore: Springer, 2017.

[31] W. Xu, X. G. Huang, and J. S. Pan, "Simple fiber-optic refractive index sensor based on Fresnel reflection and optical switch," *IEEE Sensors J.*, vol. 13, no. 5, pp. 1571–1574, May 2012.

[32] S. A. Kalogirou, *Solar Thermal Systems: Components and Applications-Introduction*. Amsterdam, The Netherlands: Elsevier, 2012.

[33] P. T. Inc. (2015). *Collaborative Data Science*. Montreal, QC, Canada. [Online]. Available: https://plot.ly

[34] S. Huo, B. Zhang, M. Muddassir, D. T. W. Chik, and D. Navarro-Alarcon, "A sensor-based robotic line scan system with adaptive ROI for inspection of defects over convex free-form specular surfaces," *IEEE Sensors J.*, vol. 22, no. 3, pp. 2782–2792, Feb. 2021.

[35] Z. Zhang, "A flexible new technique for camera calibration," *IEEE Trans. Pattern Anal. Mach. Intell.*, vol. 22, no. 11, pp. 1330–1334, Nov. 2000.

[36] B. Lu, B. Li, Q. Dou, and Y. Liu, "A unified monocular camera-based and pattern-free hand-to-eye calibration algorithm for surgical robots with RCM constraints," *IEEE/ASME Trans. Mechatronics*, early access, May 25, 2022, doi: 10.1109/TMECH.2022.3166522.

[37] G. Bradski, "The OpenCV library," *Dr. Dobb's J. Softw. Tools*, vol. 25, no. 11, pp. 120–125, 2000.

[38] *Staring Directly at the Sun Since 2007*. Accessed: Aug. 8, 2022. [Online]. Available: https://pysolar.readthedocs.io/en/latest/

[39] T. Zhang, L. Hu, L. Li, and D. Navarro-Alarcon, "Towards a multispectral RGB-IR-UV-D vision system—Seeing the invisible in 3D," in *Proc. IEEE Int. Conf. Robot. Biomimetics (ROBIO)*, Dec. 2021, pp. 1723–1728.

[40] B. Lu et al., "A learning-driven framework with spatial optimization for surgical suture thread reconstruction and autonomous grasping under multiple topologies and environmental noises," in *Proc. IEEE/RSJ Int. Conf. Intell. Robots Syst. (IROS)*, Oct. 2020, pp. 3075–3082.

[41] M. Li, Y. Chu, H. T. C. Pedro, and C. F. M. Coimbra, "Quantitative evaluation of the impact of cloud transmittance and cloud velocity on the accuracy of short-term DNI forecasts," *Renew. Energy*, vol. 86, pp. 1362–1371, Feb. 2016.

[42] Y. Hu et al., "Nonlinear model predictive control for mobile medical robot using neural optimization," *IEEE Trans. Ind. Electron.*, vol. 68, no. 12, pp. 12636–12645, Dec. 2021.

[43] O. Zahra, S. Tolu, P. Zhou, A. Duan, and D. Navarro-Alarcon, "A bio-inspired mechanism for learning robot motion from mirrored human demonstrations," *Frontiers Neurorobot.*, vol. 16, no. 826410, pp. 1–16, Mar. 2022.

[44] A. Duan et al., "Learning to sequence multiple tasks with competing constraints," in *Proc. IEEE/RSJ Int. Conf. Intell. Robots Syst. (IROS)*, Nov. 2019, pp. 2672–2678.

[45] M. Li, Z. Liao, and C. F. M. Coimbra, "Spectral solar irradiance on inclined surfaces: A fast Monte Carlo approach," *J. Renew. Sustain. Energy*, vol. 12, no. 5, Sep. 2020, Art. no. 053705.

Mengying Li received the Ph.D. degree in mechanical and aerospace engineering from the University of California at San Diego (UC San Diego), La Jolla, CA, USA, in 2018.

From 2018 to 2020, she was a Postdoctoral Scholar with the Center for Energy Research, UC San Diego. In 2020, she joined the Department of Mechanical Engineering, The Hong Kong Polytechnic University, Hong Kong, as an Assistant Professor. Her research interests include atmospheric radiative heat transfer for renewable energy integration and design of multigeneration systems.

Andrea Cherubini received the M.Sc. degree in mechanical engineering from the University of Rome La Sapienza, Rome, Italy, in 2001, the M.Sc. degree in control systems from the University of Sheffield, Sheffield, U.K., in 2003, and the Ph.D. degree in control systems from the University of Rome La Sapienza in 2008.

From 2008 to 2011, he held a postdoctoral position at INRIA Rennes, Rennes, France. Since 2021, he has been a Full Professor with the Université de Montpellier, Montpellier, France. His research interests include physical human–robot interaction and manipulation of soft objects.

Lu Li received the Diploma and Ph.D. degrees in mechanical engineering from the Hefei University of Technology, Hefei, China, in 2003 and 2010, respectively.

In 2010, she joined the Hefei Institutes of Physical Science, Chinese Academy of Sciences, Changzhou, China, as an Assistant Research Fellow, where she became an Associate Research Fellow in 2015. Her research interests include the design and control of robotic systems, legged robots, and human–machine interactive systems.

Luyin Hu received the B.Eng. and M.Phil. degrees in mechanical engineering from The Hong Kong Polytechnic University (PolyU), Hong Kong, in 2019 and 2022, respectively.

He was a Research Assistant with the Robotics and Machine Intelligence Laboratory, PolyU. His research interests include multimodal robot perception, servomechanisms, and control system design.
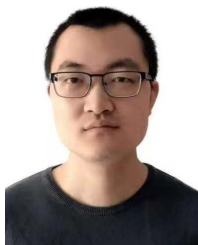
Anqing Duan received the Ph.D. degree in robotics from the Italian Institute of Technology, Genoa, Italy, and the University of Genoa, Genoa, in 2021.

He is currently a Research Associate with the Robotics and Machine Intelligence Laboratory, The Hong Kong Polytechnic University, Hong Kong. His research interest lies in robot learning and control.

David Navarro-Alarcon (Senior Member, IEEE) received the master's degree in robotics from the Centre for Research and Advanced Studies, National Polytechnic Institute, Mexico City, Mexico, in 2009, and the Ph.D. degree in mechanical and automation engineering from the Chinese University of Hong Kong (CUHK), Hong Kong, in 2014.

From 2014 to 2017, he was a Postdoctoral Fellow and then a Research Assistant Professor at the CUHK T Stone Robotics Institute, Hong Kong. Since 2017, he has been with The Hong Kong Polytechnic University, Hong Kong, where he is currently an Assistant Professor at the Department of Mechanical Engineering and the Principal Investigator of the Robotics and Machine Intelligence Laboratory. His current research interests include perceptual robotics and control theory.